

Generalization capabilities of MeshGraphNets to unseen geometries for fluid dynamics

Robin Schmöcker¹, Alexander Henkes², Julian Roth¹, and Thomas Wick^{1,3}

¹Leibniz Universität Hannover, Institut für Angewandte Mathematik, AG Wissenschaftliches Rechnen, Welfengarten 1, 30167 Hannover, Germany

²Computational Mechanics Group, ETH Zürich, Switzerland

³Université Paris-Saclay, CentraleSupélec, ENS Paris-Saclay, CNRS, LMPS - Laboratoire de Mécanique Paris-Saclay, 91190 Gif-sur-Yvette, France

Abstract

This work investigates the generalization capabilities of MeshGraphNets (MGN) [Pfaff et al. Learning Mesh-Based Simulation with Graph Networks. ICML 2021] to unseen geometries for fluid dynamics, e.g. predicting the flow around a new obstacle that was not part of the training data. For this purpose, we create a new benchmark dataset for data-driven computational fluid dynamics (CFD) which extends DeepMind’s flow around a cylinder dataset by including different shapes and multiple objects. We then use this new dataset to extend the generalization experiments conducted by DeepMind on MGNs by testing how well an MGN can generalize to different shapes. In our numerical tests, we show that MGNs can sometimes generalize well to various shapes by training on a dataset of one obstacle shape and testing on a dataset of another obstacle shape.

1 Introduction

For many engineering applications, we need to have fast and accurate simulations of fluid dynamics. In this work we focus on the modeling of fluids by the incompressible Navier-Stokes equations [28, 66, 55, 30, 68, 31, 25, 40]. With regard to numerical modeling, various spatial discretization techniques are known such as the finite volume method [50] and the finite element method [30]. Temporal discretization is often based on finite difference schemes [31, 68] or space-time discretizations [49, 11, 5]. The arising nonlinear and linear systems are often solved with iterative techniques or multigrid schemes. Implementations on CPUs can be computationally expensive and can take a long time to run. To overcome this, we can use parallelization to multiple processors or GPUs [67, 39, 6, 5] or only refine the mesh in regions where the solution is not accurate enough [10, 14, 11, 56]. Nevertheless, even though this can speed up the simulation, fluid simulations can still be prohibitively expensive for multi-query problems, e.g. different material parameters, different geometries, or different boundary conditions.

Therefore, for real-time simulations or multi-query problems, we need to find a way to speed up the simulation even further, e.g. by means of data-driven methods. A popular method to reduce the

computational cost is to collect a large dataset of fluid simulations and project the dynamics onto a small set of eigen modes using the proper orthogonal decomposition [58]. On the one hand, using this kind of reduced order model is well-studied and we have error bounds for the reduced basis approximation [57]. On the other hand, proper orthogonal decomposition is an intrusive method, which makes it difficult to implement for nonlinear problems [9, 19, 20, 24, 7, 51, 4] and changing meshes [33].

Another approach is to use machine learning methods to predict the fluid dynamics [44]. This kind of approaches are appealing since they are generally non-intrusive and easier to implement, but they can be difficult to interpret [26, 70, 63, 15], can be sensitive to the training data and can be difficult to generalize to unseen data [52]. Albeit all these limitations, neural networks are frequently used for regression in the latent space [37], superresolution of coarse solutions [48] or physics-informed approaches [18]. More recently, convolutional neural networks have been used to learn the full solution field of fluid simulations [42]. Despite their success in computer vision tasks [43], convolutional neural networks work best on cartesian grids and not for complex geometries, e.g. random obstacles in the flow field, where parts of the neural network input that is not part of the domain needs to be masked [34]. To overcome this restriction of architectures that are based on cartesian grids, like convolutional neural networks or fourier neural operators, graph neural networks [17, 16, 60] can be used to directly work on the finite element mesh [47].

In this work, we will focus on a graph neural network-based solution introduced by Google DeepMind [59, 54]. The method is based on the idea of encoding the system state into a mesh graph, applying a graph neural network to this graph to predict the change of the system, and then applying this change to the simulation state. This method has found wide adoption for physics simulations with applications in weather forecasting (GraphCast) [45] and multiscale simulations for better efficiency [27]. The application of these neural networks is usually to inverse problems [2] or for fast fluid simulations on unseen geometries [21, 69]. The latter is the focus of this work. We numerically investigate the generalization capabilities [64] of MeshGraphNets to unseen geometries for fluid dynamics by predicting the flow around a new obstacle that was not part of the training data. For this purpose we create new benchmark datasets [13] for the instationary incompressible Navier-Stokes equations that extend DeepMind’s flow around a cylinder dataset by including different shapes and multiple objects.

The outline of this paper is as follows. In Section 2, we introduce neural networks, MeshGraphNets method and the Navier-Stokes equations. Next, in Section 3, we present the experiment setup and discuss the generalization of MeshGraphNets that have been trained on one obstacle shape to another obstacle shape. Our work is summarized in Section 4.

2 MeshGraphNets

We briefly recapitulate the MeshGraphNets (MGN) method introduced by Pfaff et al. in [54]. MGNs are a deep learning approach for predicting the evolution of complex physics systems by applying graph neural networks to a mesh graph. The method is based on the idea of encoding the system state into a mesh graph, applying a graph neural network to this graph to predict the change of the system, and then applying this change to the simulation state. The method is autoregressive, meaning that the

previous output can be used as the new input, allowing for the simulation to be rolled out to obtain the next states. The method is trained using a differentiable loss function and noise is added to the training data to force the MGN to correct any mistakes before they can accumulate in future states.

We first give an abstract definition of neural networks and then introduce the concept of MGNs for fluid dynamics simulations governed by the Navier-Stokes equations.

2.1 Neural Networks

An artificial neural network (ANN) is a parametrized, nonlinear function composition. By the *universal function approximation theorem* [38], arbitrary Borel measurable functions can be approximated by ANN. There are several different formulations for ANN, which can be found in standard references such as [12, 32, 1, 29, 22]. Following [35], most ANN formulations can be unified. An ANN \mathcal{N} is a function from an *input space* \mathbb{R}^{d_x} to an *output space* \mathbb{R}^{d_y} , defined by a composition of nonlinear functions $\mathbf{h}^{(l)}$, such that

$$\begin{aligned} \mathcal{N} : \mathbb{R}^{d_x} &\rightarrow \mathbb{R}^{d_y} \\ \mathbf{x} \mapsto \mathcal{N}(\mathbf{x}) &= \mathbf{h}^{(l)} \circ \dots \circ \mathbf{h}^{(0)} = \mathbf{y}, \quad l = 1, \dots, n_L. \end{aligned} \quad (1)$$

Here, \mathbf{x} denotes an *input vector* of dimension d_x and \mathbf{y} an *output vector* of dimension d_y . The nonlinear functions $\mathbf{h}^{(l)}$ are called *layers* and define an l -fold composition, mapping input vectors to output vectors. Consequently, the first layer $\mathbf{h}^{(0)}$ is defined as the *input layer* and the last layer $\mathbf{h}^{(n_L)}$ as the *output layer*, such that

$$\mathbf{h}^{(0)} = \mathbf{x} \in \mathbb{R}^{d_x}, \quad \mathbf{h}^{(n_L)} = \mathbf{y} \in \mathbb{R}^{d_y}. \quad (2)$$

The layers $\mathbf{h}^{(l)}$ between the input and output layer, called *hidden layers*, are defined as

$$\mathbf{h}^{(l)} \triangleq \mathbf{h}_{\bullet}^{(l)} = \left\{ h_{\bullet, \eta}^{(l)}, \eta = 1, \dots, n_u \right\}, \quad h_{\bullet, \eta}^{(l)} = \varphi^{(l)} \circ \phi^{(l)} \left(\mathbf{W}_{\eta}^{(l)} \bullet \mathbf{h}^{(l-1)} \right), \quad (3)$$

where $h_{\bullet, \eta}^{(l)}$ is the η -th *neural unit* of the l -th layer $\mathbf{h}_{\bullet}^{(l)}$ and n_u is the *total number of neural units per layer*, while \bullet denotes a product. Following the notation in [41], the symbol \triangleq denotes an abbreviation of a tuple of mathematical objects $(\mathcal{O}_1, \mathcal{O}_2, \dots)$, such that $\mathcal{O} \triangleq (\mathcal{O}_1, \mathcal{O}_2, \dots)$. In (3), the details of type-specific layers $\mathbf{h}_{\bullet}^{(l)}$ are gathered in general layers $\mathbf{h}^{(l)}$ from (1). The specification follows from the \bullet -operator, which denotes the operation between the *weight vector* $\mathbf{W}_{\eta}^{(l)}$ of the η -th neural unit in the l -th layer $\mathbf{h}_{\bullet}^{(l)}$ and the output of the preceding layer $\mathbf{h}_{\bullet}^{(l-1)}$, where the bias term is absorbed [1]. If \bullet is the ordinary matrix multiplication $\bullet = \cdot$, then the layer $\mathbf{h}^{(l)}$ is called *dense layer*. In the context of GNNs, the choice of the operator as $\bullet = \oplus$, where \oplus is a permutation invariant aggregation operator, yields the so-called *message passing network* [16].

Furthermore, $\phi^{(l)} : \mathbb{R} \rightarrow \mathbb{R}$ is a nonlinear *activation function* and $\varphi^{(l)}$ is a function of the previous layer, such that $\varphi^{(l)} : \mathbf{h}^{(l-1)} \mapsto \varphi^{(l)}(\mathbf{h}^{(l-1)})$. If $\varphi^{(l)}$ is the identity function, the layer $\mathbf{h}^{(l)}$ is called a *feedforward layer*. All weight vectors $\mathbf{W}_{\eta}^{(l)}$ of all layers $\mathbf{h}^{(l)}$ can be gathered in a single expression, such

that

$$\boldsymbol{\theta} = \left\{ \mathbf{W}_\eta^{(l)} \right\}, \quad (4)$$

where $\boldsymbol{\theta}$ inherits all parameters of the ANN $\mathcal{N}(\mathbf{x})$ from (1). Consequently, the notation $\mathcal{N}(\mathbf{x}; \boldsymbol{\theta})$ emphasises the dependency of the outcome of an ANN on the input on the one hand and the current realization of the weights on the other hand. The specific combination of layers $\mathbf{h}_\bullet^{(l)}$ from (3), neural units $h_{\bullet, \eta}^{(l)}$ and activation functions $\phi^{(l)}$ from (3) is called *topology* of the ANN $\mathcal{N}(\mathbf{x}; \boldsymbol{\theta})$. The weights $\boldsymbol{\theta}$ from (4) are typically found by gradient-based optimization with respect to a task-specific *loss function* [32].

2.2 Mesh Graph Networks

In this section, we introduce MGN, a deep learning approach for predicting the evolution of complex physics systems by applying graph neural networks to a mesh graph. This is based on the paper [54] by Pfaff et al. which is an extension of their previous paper on graph network based simulations [59]. In the following and overall in this paper, we introduce and test MGNs for the Flow around the Cylinder benchmark (abbreviated as Cylinder Flow). However, we notice that our developments can be applied to other computational fluid dynamics numerical tests as well.

2.2.1 Incompressible Navier-Stokes equations

Let $\Omega \subset \mathbb{R}^2$ be some domain with sufficiently smooth boundary $\partial\Omega$. Moreover, let $(0, T)$ be the time interval with end time value $T > 0$. To generate training data, we model incompressible, viscous fluid flow with constant density and temperature by the Navier-Stokes equations

$$\begin{aligned} \partial_t \mathbf{v} - \nabla_x \cdot \boldsymbol{\sigma} + (\mathbf{v} \cdot \nabla_x) \mathbf{v} &= 0 \quad \text{in } \Omega \times (0, T), \\ \nabla_x \cdot \mathbf{v} &= 0 \quad \text{in } \Omega \times (0, T), \\ \mathbf{v} &= \mathbf{v}_D \quad \text{on } \partial\Omega \times (0, T), \\ \mathbf{v}(0) &= \mathbf{v}^0 \quad \text{in } \Omega \times \{0\}, \end{aligned}$$

where for the stress $\boldsymbol{\sigma}$ we use the unsymmetric stress tensor

$$\boldsymbol{\sigma} := \boldsymbol{\sigma} \begin{pmatrix} \mathbf{v} \\ p \end{pmatrix} = -pI + \nu \nabla_x \mathbf{v}.$$

Plugging the definition of the unsymmetric stress tensor into the Navier-Stokes equations leads to the following formulation:

Formulation 2.1 (Incompressible Navier-Stokes equations). *Find the vector-valued velocity $\mathbf{v} : \Omega \times$*

$(0, T) \rightarrow \mathbb{R}^2$ and the scalar-valued pressure $p : \Omega \times (0, T) \rightarrow \mathbb{R}$ such that

$$\begin{aligned}\partial_t \mathbf{v} + \nabla_x p - \nu \Delta_x \mathbf{v} + (\mathbf{v} \cdot \nabla_x) \mathbf{v} &= 0 \quad \text{in } \Omega \times (0, T), \\ \nabla_x \cdot \mathbf{v} &= 0 \quad \text{in } \Omega \times (0, T), \\ \mathbf{v} &= \mathbf{v}_D \quad \text{on } \partial\Omega \times (0, T), \\ \mathbf{v}(0) &= \mathbf{v}^0 \quad \text{in } \Omega \times \{0\}.\end{aligned}$$

Here, $\nu > 0$ is the kinematic viscosity, \mathbf{v}^0 is the initial velocity and \mathbf{v}_D is a possibly time-dependent Dirichlet boundary value. In the following, we directly address the time-discrete problem. To this end, $\mathbf{s}_k = (\mathbf{v}_k, p_k) : \bar{\Omega} \mapsto \mathbb{R}^3$ denotes the system state (i.e. the velocity and pressure field) with domain $\Omega \subseteq \mathbb{R}^2$ at time $\Delta t \cdot k$ with the time step size $\Delta t > 0$ and the time step index $k \in \mathbb{N}$. Additionally, we use $\tilde{\mathbf{s}}_k = (\tilde{\mathbf{v}}_k, \tilde{p}_k) : \bar{\Omega} \mapsto \mathbb{R}^3$ to denote our prediction for \mathbf{s}_k . To create the dataset, we employ the finite element method using an *incremental pressure correction scheme* (IPCS) [46] which is based on Chorin’s method [23].

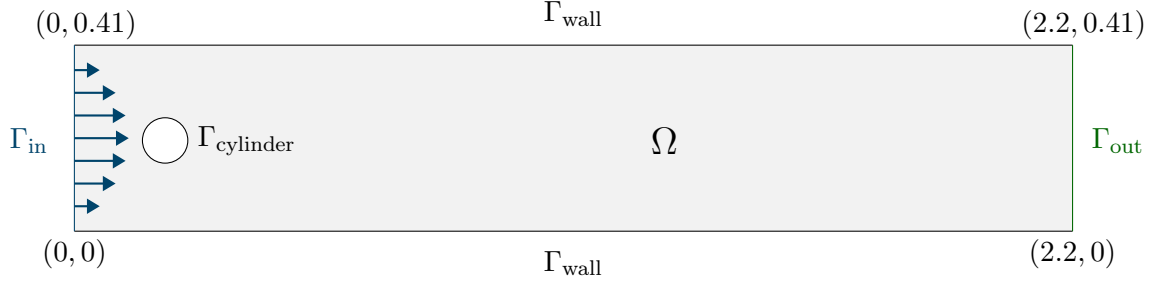


Figure 1: Domain of the Navier-Stokes benchmark problem (Cylinder Flow) [62]

2.2.2 MGN idea

On a high level, the MGN approach can be explained as follows: First, we triangulate the domain to represent it as a mesh graph. We then encode the current system state \mathbf{s}_k into the graph’s nodes and edges. Next, we use a graph neural network to predict quantities which can be used to directly compute how \mathbf{s}_k evolves to \mathbf{s}_{k+1} . In Cylinder Flow, we will use an MGN to directly predict the pressure field p_{k+1} , and the change in velocity $\delta \mathbf{v} = \mathbf{v}_{k+1} - \mathbf{v}_k$. Fig. 2 visualizes this process.

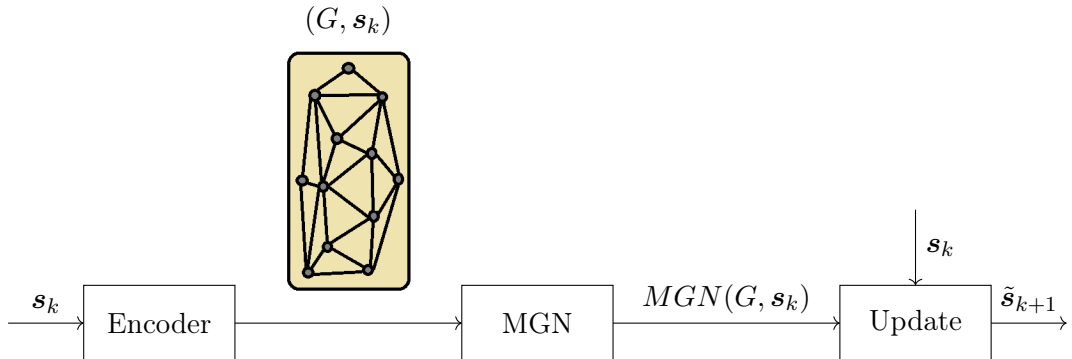


Figure 2: High-level overview of how MGNS predict the next state given the current state \mathbf{s}_k .

By construction, MGNs are autoregressive which means we can use the previous output as new input. Hence we can rollout a state \mathbf{s}_k to obtain $\mathbf{s}_{k+1}, \mathbf{s}_{k+2}, \dots$. We will now discuss this on a more detailed level.

2.2.3 System state encoding

In this step, we want to encode the system state \mathbf{s}_k into a graph. As a first step, the domain $\bar{\Omega}$ has to be triangulated to obtain a mesh graph $G = (V, E)$ where $V \subseteq \mathbb{N}$ are the vertices and $E \subseteq \{\mathbf{e} \in \mathcal{P}(V) : |\mathbf{e}| = 2\}$ are the edges.

Next, we encode the position information into the graph: Let $\mathbf{e} = \{\nu_1, \nu_2\} \in E$ and $\mathbf{x}_{\nu_1}, \mathbf{x}_{\nu_2} \in \bar{\Omega}$ be the domain coordinates associated with these two vertices. We assign the distance $\|\mathbf{x}_{\nu_1} - \mathbf{x}_{\nu_2}\|_2$ and the relative displacement $\mathbf{x}_{\nu_1} - \mathbf{x}_{\nu_2}$ as features to \mathbf{e} . It would also be possible to encode the absolute positions in the nodes. Experiments showed, however, that this is not a viable option [54]. To better capture the structure of the mesh, the node type is added as a feature to each vertex. In the case of Cylinder Flow there are four types of nodes:

- fluid nodes,
- wall (top, bottom, and cylinder) nodes,
- inflow nodes,
- outflow nodes.

Besides the node type we also add the values of the fields of \mathbf{s}_k needed to predict \mathbf{s}_{k+1} as features to each vertex. For example, in the case of Cylinder Flow, each vertex $\nu \in V$ with associated coordinates $\mathbf{x} \in \bar{\Omega}$ gets the value of the velocity field \mathbf{v}_k at position \mathbf{x} . Though pressure is also part of \mathbf{s}_k , it is not encoded as \mathbf{v}_k already determines the pressure values hence they are not needed to predict \mathbf{s}_{k+1} . The resulting graph and its associated features now approximately model \mathbf{s}_k .

2.2.4 Graph processing

In this step, we use the graph-encoding of the previous step to predict \mathbf{s}_{k+1} . For the incompressible Navier-Stokes equations, we directly predict the pressure p_{k+1} and the change in velocity $\delta \mathbf{v} = \mathbf{v}_{k+1} - \mathbf{v}_k$. The processing is done in three different steps.

1. First, to prepare the features for processing, we use a feedforward-network to encode the edge features and another feedforward-network to encode the vertex features at each edge/vertex. We say that the features are embedded into latent space. In theory, this step is not needed. However, in practice without this step, the network would not perform well. This is because in the next step, these features will iteratively be updated to finally arrive at the prediction for the quantity change. If we do not encode the features in this first step, the information captured in these intermediate states is always restricted to the dimension of the input features. Therefore, this step can be viewed as widening the information bottleneck.

2. Next, we process the previously encoded features. First, we apply a neural network \mathcal{N}^M to all edges to update their edge features. Let $\mathbf{e} = \{\nu_1, \nu_2\} \in E$ and $\mathcal{F}(\nu_1), \mathcal{F}(\nu_2), \mathcal{F}(\mathbf{e})$ be the features associated with this edge/nodes. The updated edge features $\mathcal{F}'(\mathbf{e})$ are given as follows:

$$\mathcal{F}'(\mathbf{e}) = \mathcal{N}^M(\mathcal{F}(\mathbf{e}), \mathcal{F}(\nu_1), \mathcal{F}(\nu_2)). \quad (5)$$

Using $\mathcal{F}'(\mathbf{e})$, we update the node-features using another neural network \mathcal{N}^V . Let $\nu \in V$ and $N_\nu \subseteq E$ be the set of edges connected to ν . Again, we denote their associated features with $\mathcal{F}(\nu)$ and $\mathcal{F}'(\mathbf{e})$ for $\mathbf{e} \in N_\nu$. The updated features $\mathcal{F}'(\nu)$ are defined as follows:

$$\mathcal{F}'(\nu) = \mathcal{N}^V \left(\mathcal{F}(\nu), \sum_{\mathbf{e} \in N_\nu} \mathcal{F}'(\mathbf{e}) \right). \quad (6)$$

After this, we simply replace $\mathcal{F}(\nu)$ by $\mathcal{F}'(\nu)$ and $\mathcal{F}(\mathbf{e})$ by $\mathcal{F}'(\mathbf{e})$ for each vertex/edge. This is called one *message passing block* (MPB). In total, we apply L identical message passing blocks to the features (i.e. $\mathcal{N}^M, \mathcal{N}^V$ are fixed).

Note that within each message passing block, information can flow only from one vertex to all its neighbors, because its information first passes to its edges by \mathcal{N}^M and then to its neighbors by \mathcal{N}^V . Hence with L MPBs only vertices with a distance of less than L steps can be reached which means that even though in theory nodes can influence each other no matter their distance, this is not captured by this processing step.

3. In this last step, we apply a final feedforward-net (called the decoder) to the latent features of each vertex obtained after the last MPB step. This output will then be used to directly update the system state as will be described in the following.

2.2.5 Updating the system state

Assume that $\mathbf{q}_{k+1} : V \mapsto \mathbb{R}^3$ is the output of our MGN with input \mathbf{s}_k . We interpret \mathbf{q}_{k+1} as the derivative of the velocity field \mathbf{v}_k and the pressure p_{k+1} , i.e. $\mathbf{q}_{k+1} = (\mathbf{q}_{1,k+1}, q_{2,k+1}) \approx (\partial_t \mathbf{v}_k, p_{k+1})$ where $\partial_t \mathbf{v}_k$ denotes the time derivative of the velocity field at time $\Delta t \cdot k$. Our prediction $\tilde{\mathbf{s}}_{k+1}$ at node $\nu \in V$ with coordinates $\mathbf{x} \in \bar{\Omega}$ is then given by

$$\tilde{\mathbf{s}}_{k+1}(\mathbf{x}) = (\mathbf{v}_k(\mathbf{x}) + \Delta t \cdot \mathbf{q}_{1,k+1}(\nu), q_{2,k+1}(\nu)). \quad (7)$$

2.2.6 Training MGNs

In this section, we discuss the training details of MGNs. First, note that each step as detailed in the previous section is differentiable. Hence, the predicted quantities at each vertex are differentiable with respect to the parameters of all neural networks that were used. Therefore, we can define a differentiable loss \mathcal{L} at each node $\nu \in V$ with coordinates $\mathbf{x} \in \bar{\Omega}$ by taking the mean-squared-error of the MGN

prediction and the ground truth field values. Hence, the loss \mathcal{L} is

$$\mathcal{L}(\nu) = \frac{1}{3} \|\tilde{\mathbf{s}}_{k+1}(\mathbf{x}) - \mathbf{s}_{k+1}(\mathbf{x})\|_2^2. \quad (8)$$

The MGN can then be trained using gradient descent on \mathcal{L} averaged on each vertex. Note that this requires access to the ground truth values \mathbf{s}_k at the vertices or approximations of these which might not always be efficiently available.

Though this training setup works in theory, experiments [54] showed that this does not suffice to predict states far in the future and not just the next time step. This problem is addressed by adding noise to the training data and thus forcing the MGN to correct any mistakes before they can accumulate in future states. For all simulations in the training data, at every time step k and at each vertex $\nu \in V$ with coordinates $\mathbf{x} \in \overline{\Omega}$, we independently sample normally distributed noise $\boldsymbol{\varepsilon} = (\varepsilon_1, \varepsilon_2)$ with $\varepsilon_1, \varepsilon_2 \sim \mathcal{N}(0, \sigma)$ with zero mean and a fixed variance $\sigma \in \mathbb{R}^+$. This noise is then added to the velocity field $\mathbf{v}_k(\mathbf{x})$ to obtain the noisy velocity field $\mathbf{v}_k^{noisy}(\mathbf{x}) = \mathbf{v}_k(\mathbf{x}) + \boldsymbol{\varepsilon}$. Then, instead of \mathbf{v}_k , the noisy velocity field \mathbf{v}_k^{noisy} is fed as the input to the MGN whose next state prediction we then denote by $\tilde{\mathbf{s}}_{k+1}^{noisy}$ which is then used in Equation (8) instead of $\tilde{\mathbf{s}}_{k+1}$. The target \mathbf{s}_{k+1} remains unchanged. This modification allows the MGN to learn how to denoise the system state thereby learning how to reduce error accumulation as shown experimentally by DeepMind [54].

3 Generalization Capabilities of MeshGraphNets and Numerical Simulations

In this section, we will present experimental results on the generalization of MGNs to unseen datasets. First, in Section 3.1 we will describe our experiment setup. Then, in Section 3.2 we will present the datasets of the generalization experiments, followed by the results in Section 3.3 and the runtimes in Section 3.4. The code used for these experiments is publicly available [65].

3.1 Setup of the experiments

In this section, we will describe the exact setup for the MGNs used for the generalization experiments. We will also describe which evaluation metrics for the MGNs were used for the subsequent experiments.

3.1.1 Implementation

For the generalization experiments, we use the implementation contained in NVIDIA’s Modulus, a machine learning framework for physics [36, 53]. More specifically, the exact implementation contained in `examples/cfd/vortex_shedding_mgn`¹ from NVIDIA Modulus [53] was used for experimentation with modifications only affecting logging and the learning rate schedule which is now only updated after every epoch such that the learning rate in epoch l is $\eta_1 \gamma^{l-1}$ for some initial learning rate η_1 and learning rate decay γ .

¹https://github.com/NVIDIA/modulus/tree/main/examples/cfd/vortex_shedding_mgn

3.1.2 MGN architecture details

We highlight some notable architectural choices of the MGNs.

- Input and target normalization: The training data set is used to compute the mean and variance of all edge features and of the velocity and pressure for the node features. The features of all inputs and targets are then normalized using their corresponding mean and variance.
- Residual connections: The MGN will be extremely deep, therefore residual connections are added such that the input of each MBP is directly added to its output.
- Layer normalization: Since we will be using a batch size of one but still want to normalize the hidden-layer outputs to reduce the covariate shift (i.e. gradients in layer i tend to highly depend on the outputs of layer $i - 1$), we employ layer normalization [8] at the output of the edge/node encoder and after each MPB (before the residual connection). Layer normalization transforms an output $x \in \mathbb{R}^n$ as follows:

$$y = \frac{x - \mathbb{E}[x]}{\sqrt{\text{Var}[x] + \epsilon}} \cdot \alpha + \beta \quad (9)$$

where $\mathbb{E}[x]$ is subtracted componentwise and

$$\mathbb{E}[x] = \frac{1}{n} \sum_{i=1}^n x_i, \quad \text{Var}[x] = \frac{1}{n} \sum_{i=1}^n (x_i - \mathbb{E}[x])^2 \quad (10)$$

where $\alpha, \beta \in \mathbb{R}$ are learnable parameters and $\epsilon > 0$ for numerical stability. We used $\epsilon = 10^{-5}$.

3.1.3 Hyperparameters

The exact hyperparameters from `examples/cfd/vortex_shedding_mgn`² from NVIDIA Modulus [53] were used for the subsequent experiments. The only exception is the learning rate decay factor γ since we used a slightly different implementation of the learning rate decay schedule as described in Subsection 3.1.1. Table 1 lists the hyperparameters.

²https://github.com/NVIDIA/modulus/tree/main/examples/cfd/vortex_shedding_mgn

Parameter	Value	Comment
Epochs	25	Iterate entire dataset per epoch
Batch size	1	
Initial learning rate η_1	0.0001	$\eta_l = \eta_1 \gamma^{l-1}$ at epoch l .
Learning rate decay γ	0.82540	
Message passing blocks L	15	
Encoders/Decoder/Processors hidden layers	2	
Encoders/Decoder/Processors hidden dim	128	
Node embedding size	128	PyTorch v1.11.0
Edge embedding size	128	
Activation function	ReLU	
Optimizer	Adam	
Parameter initialization	PyTorch default	
Training noise	$\mathcal{N}(0, 0.02)$	

Table 1: Hyperparameters used for the experiments.

3.1.4 Evaluation criteria

For each experiment, we use at least 10% of the total dataset for evaluation. The exact evaluation datasets will be mentioned in the corresponding experiment. Let $K \in \mathbb{N}$ denote the number of simulations, let $J \in \mathbb{N}$ denote the number of time steps in each simulation, and let $I_k \in \mathbb{N}$ denote the number of mesh nodes in the k -th simulation with $k \leq K$ of the evaluation dataset. For evaluation, we measure eight quantities. The first four are derived from the root-mean-squared-error (RMSE) of the velocity. Let $v_{i,j,k} \in \mathbb{R}^2$ denote the velocity vector at mesh node $i \leq I_k$ and time step $j \leq J$ in the k -th ($k \leq K$) simulation of the evaluation dataset obtained by performing the IPCS (more details on the dataset generation in the next section). Furthermore, we use $\tilde{v}_{i,j,k}$ to denote the MGN velocity prediction from $v_{i,j-1,k}$ if $j > 1$ and $v_{i,1,k}$ if $j = 1$. Lastly, by $\hat{v}_{i,j,k}$ we denote the MGN velocity prediction from $\tilde{v}_{i,j-1,k}$ if $j > 1$ and $v_{i,1,k}$ if $j = 1$. From which MGN the predictions come will be specified every time one of the following error quantities is reported.

- **Velocity 1-step error $\epsilon_1^{(v)}$** : This error is the RMSE for all the next state velocity predictions of all timesteps of all simulations which is given by

$$\epsilon_1^{(v)} = \sqrt{\sum_{k=1}^K \sum_{j=1}^J \sum_{i=1}^{I_k} \frac{\|v_{i,j,k} - \tilde{v}_{i,j,k}\|_2^2}{2I_k \cdot J \cdot K}}. \quad (11)$$

- **Velocity 50-steps error $\epsilon_{50}^{(v)}$** : Each simulation is rolled out for 50 timesteps. The RMSE is then taken for the rollout velocity at each of the first 50 time steps compared to the IPCS result for all simulations. This given by

$$\epsilon_{50}^{(v)} = \sqrt{\sum_{k=1}^K \sum_{j=1}^{50} \sum_{i=1}^{I_k} \frac{\|v_{i,j,k} - \hat{v}_{i,j,k}\|_2^2}{2I_k \cdot 50 \cdot K}}. \quad (12)$$

- **Velocity all-steps error $\epsilon_{all}^{(v)}$** : Each simulation is fully rolled out. The RMSE then compares the rollout velocity prediction at each time step to the IPCS velocity for all simulations. Formally, this is

$$\epsilon_{all}^{(v)} = \sqrt{\sum_{k=1}^K \sum_{j=1}^J \sum_{i=1}^{I_k} \frac{\|v_{i,j,k} - \hat{v}_{i,j,k}\|_2^2}{2I_k \cdot J \cdot K}}. \quad (13)$$

- **Velocity all-steps median $\epsilon_{all,median}^{(v)}$** : We first calculate the all-steps RMSE for each individual simulation $k \leq K$ as

$$\epsilon_{all,k}^{(v)} = \sqrt{\sum_{j=1}^J \sum_{i=1}^{I_k} \frac{\|v_{i,j,k} - \hat{v}_{i,j,k}\|_2^2}{2I_k \cdot J}}. \quad (14)$$

The error $\epsilon_{all,median}^{(v)}$ is then given by the median of $(\epsilon_{all,1}^{(v)}, \dots, \epsilon_{all,K}^{(v)})$.

We ran each experiment with three different seeds. For each of the above error quantities, we report the mean and the maximum deviation from the mean across all three seeds. For example, we would report the three values $\{0, 3, 12\}$ as 5 ± 7 .

The remaining four error quantities $\epsilon_1^{(p)}, \epsilon_{50}^{(p)}, \epsilon_{all}^{(p)}$, and $\epsilon_{all,median}^{(p)}$ come from doing the same with the pressure predictions.

3.2 Generalization experiments: Datasets

The experiments in this section have the aim of expanding DeepMind’s MGN generalization experiments. DeepMind claims that their MGN has strong generalization capabilities due to using a relative encoding on the mesh graphs, however, they report no experimental evidence for this for their Cylinder Flow based dataset at all [54]. Additionally, in their Airfoil experiments of compressible Navier-Stokes equations, which is a related problem to Cylinder Flow, they only test the MGN by using values for the system parameters (such as the inflow speed) that are slightly out of the training distribution. What they do not do is test the MGN on qualitatively different meshes such as one where a different shape other than a circle is used.

Therefore, in this section, we apply a trained MGN to similar but qualitatively different datasets than it was trained on in which the cylinder may be stretched or squeezed (**cylinder_stretch**), the cylinder might be replaced with a triangle or rectangle (**cylinder_tri_quad**), there could even be multiple cylinders (**2cylinders**), or all modifications mixed together (**mixed_all**) or simply no modifications (**standard_cylinder**).

The datasets consist of approximations of solutions (velocity \mathbf{v} and pressure p) to the Cylinder Flow problem. The datasets are created by varying the inflow profile or applying changes to the cylinder. Whenever possible, the distributions for the parameters we used were reverse-engineered from Google Deepmind’s dataset [54] assuming that uniform distributions were used. One notable difference to the DFG³ 2D-2 benchmark problem [62] is that the pipe is a bit shorter (1.6 instead of 2.2 length) to speed up computation. Other than that, the range of parameters includes this benchmark problem. We note that the mean values for certain quantities such as the x -position of the cylinder are not always

³DFG stands for German Research Foundation

equal to the one in the benchmark problem as we had to include some wiggle room to avoid unphysical situations (e.g. the cylinder intersects the inflow).

The domain Ω for a single simulation is always of the form $\Omega = [(0, 1.6) \times (0, 0.41)] \setminus \bar{\mathcal{C}} \subseteq \mathbb{R}^2$, where $\mathcal{C} \subseteq \mathbb{R}^2$ is distributed depending on the dataset.

- **standard_cylinder**: In this dataset \mathcal{C} is always a circle with midpoint (x, y) where $x \sim \mathcal{U}[0.15, 0.5]$ and $y \sim \mathcal{U}[0.1, 0.3]$ are sampled independently. The radius is sampled from $r \sim \mathcal{U}[0.02, 0.08]$.
- **cylinder_stretch**: Same as in **standard_cylinder** except that the circle may now be an ellipse with height $h \sim \mathcal{U}[0.02, 0.08]$ and width $w \sim \mathcal{U}[0.02, 0.08]$.
- **cylinder_tri_quad**: There is a $\frac{1}{3}$ chance that a circle as in **standard_cylinder** is chosen. There is another $\frac{1}{3}$ chance that a square with a midpoint sampled the same way as the ellipse's and side length $s \sim \mathcal{U}[0.02\sqrt{2}, 0.08\sqrt{2}]$ and a random orientation with a uniformly sampled angle is chosen. And another $\frac{1}{3}$ chance that an equilateral triangle with side length $s \sim \mathcal{U}[0.078, 0.182]$ and a random orientation with a uniformly sampled angle and midpoint sampled the same way as the ellipse's is chosen as \mathcal{C} .
- **2cylinders**: $\mathcal{C} = \mathcal{C}_1 \cup \mathcal{C}_2$. Here \mathcal{C}_1 is an object as in **standard_cylinder**. With a $\frac{1}{2}$ chance, we choose $\mathcal{C}_2 = \emptyset$ and otherwise \mathcal{C}_2 is sampled the same as \mathcal{C}_1 except that the mean-midpoint is now $(0.825, 0.2)$ instead of $(0.325, 0.2)$.
- **mixed_all**: $\mathcal{C} = \mathcal{C}_1 \cup \mathcal{C}_2$. Here \mathcal{C}_1 is an object as in **cylinder_tri_quad** except that each object is randomly stretched or squeezed (a circle is stretched as in **cylinder_stretch**, a square samples width and height independently as its side length, and a triangle stretches around its midpoint with the factor $s \sim \mathcal{U}[0.7, 1.3]$ in the x -direction and $\frac{1}{s}$ in the y -direction). With a $\frac{1}{4}$ chance \mathcal{C}_2 is sampled the same as \mathcal{C}_1 except that the midpoint is now shifted by 0.5 in the x -direction, i.e. it is now $(0.825, 0.2)$. However, with a $\frac{3}{4}$ chance we choose $\mathcal{C}_2 = \emptyset$.

All of the above-described domains are triangulated with pygmsh [61] using the parameters $mesh_size = 0.0225$ for the domain and $mesh_size = 0.0098$ for the geometric objects to have a finer mesh around the region of interest. We chose these parameters to get to a similar mesh size that DeepMind used for their dataset. Furthermore, to avoid extreme edge cases, we exclude meshes where the rectangular bounding box of the object(s) come(s) within a distance of less than 0.02 to the boundary $\partial\Omega$. For **standard_cylinder** with the circle being centered at $(0.325, 0.2)$ and $r = 0.05$ we obtain a mesh with 2069 vertices and 3924 triangles/cells. For the slightly elongated pipe of width 2.2 and circle centered at $(0.2, 0.2)$ we get 2582 vertices and 4898 cells. Note that we do not use this elongated mesh for the experiments. We will only use it later to compare quantities of interest with the benchmark results to verify our computation. Fig. 3 shows one sample mesh for each mesh set.

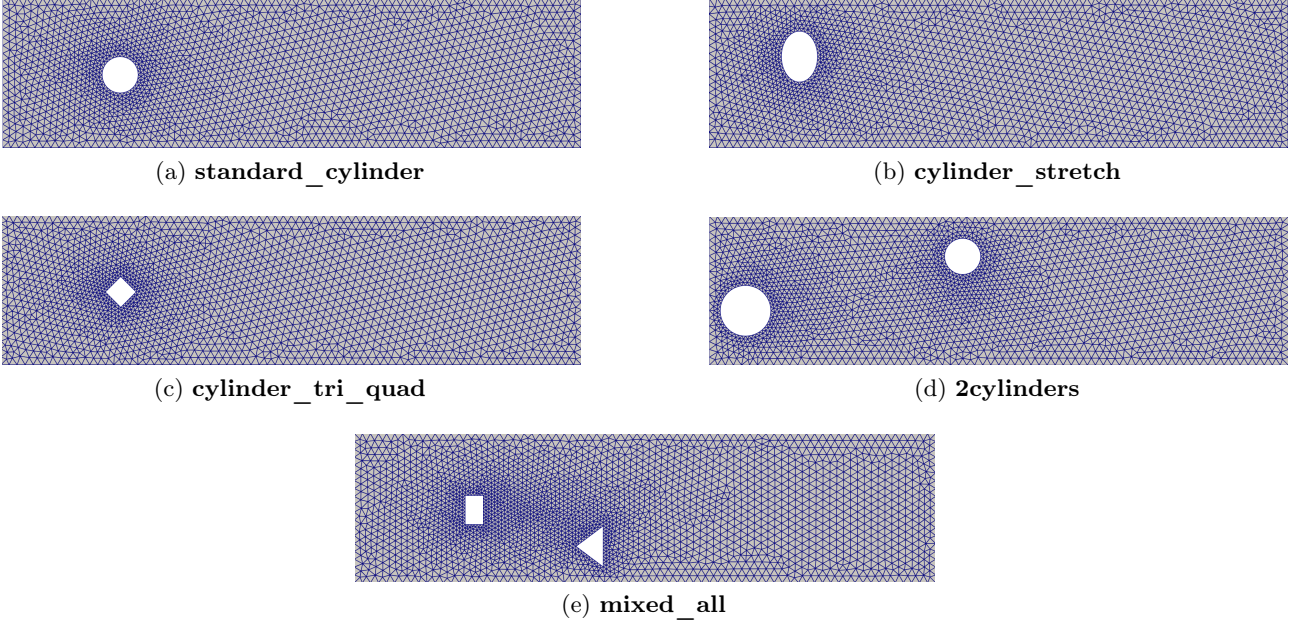


Figure 3: One example mesh from each of the five datasets.

The inflow profile is determined the same way for each mesh in each dataset. First, we sample $U \sim \mathcal{U}[0.25, 2.25]$. The inflow profile is then given by:

$$\mathbf{v}(x, y, t) = \left(U \cdot \frac{4y(0.41 - y)}{0.41^2}, 0 \right), \quad (x, y, t) \in (\{0\} \times [0, 0.41]) \times I. \quad (15)$$

For a given mesh, the solution velocity \mathbf{v} and pressure p is approximated using the IPCS. FEniCS [3] was used as the solver using inf-sup stable quadratic elements for velocity and linear elements for the pressure. Each simulation within a dataset contains the velocity and pressure values at each vertex in the mesh that was used for the approximation from $t = 0.01s$ to $t = 3s$ in $0.01s$ intervals, i.e. $t \in \{m, 2m, \dots, 300m\}$ with $m = 1/100s$. As the initial velocity for the solver, we simply used $\mathbf{v}, p \equiv 0$. Since this violates the boundary conditions, we exclude $t = 0s$ and begin with $t = 1/100s$ since at that time the boundary conditions are approximately satisfied. Even though the intervals are of size 0.01 , the solver used an adaptive Δt under the hood that scales with the inflow peak. We used $\Delta t = 0.00025$ for an inflow peak of 1.25 . In total, each dataset contains 440 simulations where 400 are used for training, and 40 for evaluation.

The above-described datasets can be generated by following the instructions provided in *README.md* of the codebase [65]. As mentioned in the introduction, these datasets combined, constitute a new benchmark for fluid simulations that extends DeepMind’s Cylinder Flow based dataset [54].

3.2.1 Comparison to DFG 2D-2 benchmark

To verify our experiment setup for generating datasets, we computed some quantities of interest and compared them to the Navier-Stokes 2D-2 benchmark results by Schäfer and Turek [62]. For this, we

simulated the flow on the pipe with width 2.2 and circle center at (0.2, 0.2) for 30 seconds to make sure that the flow was fully developed. We considered the interval $[29.9295s, 29.9625s]$ (the last interval between two maxima of the lift coefficient) for our measurements. We measured the maximum value of the drag coefficient c_D and the lift coefficient c_L within this interval and the pressure difference Δp at the interval-midpoint $t_{mid} = 29.9460s$. We ran this computation on a system with six Intel(R) Core(TM) i5-9600K @ 3.70GHz CPUs with 32 GB of RAM. Table 2 shows our results.

Quantity	Results	Benchmark results
St	3.0303	[0.2950, 0.3050]
$\max c_D$	3.1668	[3.2200, 3.2400]
$\max c_L$	1.0210	[0.9900, 1.0100]
Δp	2.5017	[2.4600, 2.5000]

Table 2: Quantities of interest for DFG 2D-2 benchmark.

We note that our values slightly deviate from the benchmark results but are still deemed acceptable.

3.3 Generalization experiments: Results

We tested the generalization capabilities of the MGNs. For this, we tested each MGN on every dataset. E.g. train on **cylinder_stretch** and evaluate on **2cylinders** and do this for every possible dataset-pair. Table 3 (resp. 4, 5, 6, 7) shows the results if an MGN was trained on all of the five datasets and evaluated on **standard_cylinder** (resp. **cylinder_stretch**, **cylinder_tri_quad**, **2cylinders**, **mixed_all**) in terms of the pressure and velocity RMSE as described in Section 3.1.4. Additionally, these tables also contain the RMSEs for newly initialized MGNs that were not trained to act as a benchmark for comparison. All reported velocity errors have been rounded to five decimal places and all pressure errors have been rounded to four decimal places.

Velocity RMSE $\times 10^{-3}$

Train Dataset	1-step	50-steps	all-steps	all-steps median
standard_cylinder	2.32 \pm 0.02	32.93 \pm 5.15	89.19 \pm 17.2	24.22 \pm 4.01
cylinder_stretch	2.56 \pm 0.01	40.0 \pm 3.67	100.52 \pm 14.05	33.97 \pm 0.64
cylinder_tri_quad	2.72 \pm 0.01	36.46 \pm 2.39	94.84 \pm 8.77	34.97 \pm 3.58
2cylinders	2.52 \pm 0.03	35.22 \pm 4.12	89.3 \pm 13.22	35.03 \pm 3.44
mixed_all	2.98 \pm 0.01	40.72 \pm 1.86	115.44 \pm 11.12	39.08 \pm 0.9
None	32.29 \pm 3.05	473.44 \pm 214.41	1398.48 \pm 618.28	1369.2 \pm 635.18

Pressure RMSE $\times 10^{-2}$

Train Dataset	1-step	50-steps	all-steps	all-steps median
standard_cylinder	6.54 \pm 0.08	5.69 \pm 0.3	10.3 \pm 0.42	1.77 \pm 0.2
cylinder_stretch	7.31 \pm 0.06	7.36 \pm 0.14	11.71 \pm 1.48	2.03 \pm 0.14
cylinder_tri_quad	9.39 \pm 0.5	9.57 \pm 0.7	12.42 \pm 1.0	2.36 \pm 0.25
2cylinders	11.58 \pm 0.94	12.45 \pm 0.99	14.27 \pm 0.86	6.34 \pm 1.06
mixed_all	12.25 \pm 0.82	13.78 \pm 0.94	16.6 \pm 0.63	3.99 \pm 0.65
None	38.84 \pm 3.83	36.2 \pm 3.89	38.34 \pm 3.09	20.77 \pm 6.11

Table 3: RMSE if evaluated on **standard_cylinder**. *None* means that a newly initialized network without any training was evaluated. The lowest RMSE of each column has been marked.

Velocity RMSE $\times 10^{-3}$

Train Dataset	1-step	50-steps	all-steps	all-steps median
standard_cylinder	7.33 \pm 0.15	54.4 \pm 9.12	199.34 \pm 10.76	55.02 \pm 12.11
cylinder_stretch	3.52 \pm 0.03	43.1 \pm 3.22	221.25 \pm 21.11	42.16 \pm 7.85
cylinder_tri_quad	4.5 \pm 0.05	53.38 \pm 7.16	217.1 \pm 30.32	40.71 \pm 6.3
2cylinders	6.15 \pm 0.12	85.71 \pm 7.76	265.68 \pm 6.82	73.28 \pm 7.94
mixed_all	3.91 \pm 0.03	56.36 \pm 6.82	210.39 \pm 13.78	42.71 \pm 5.38
None	49.51 \pm 3.23	903.62 \pm 552.82	3111.27 \pm 2347.83	3119.95 \pm 2352.9

Pressure RMSE $\times 10^{-2}$

Train Dataset	1-step	50-steps	all-steps	all-steps median
standard_cylinder	16.37 \pm 0.11	10.68 \pm 0.93	29.53 \pm 0.58	4.14 \pm 0.2
cylinder_stretch	11.46 \pm 0.03	9.03 \pm 1.31	28.65 \pm 1.87	4.1 \pm 0.26
cylinder_tri_quad	14.38 \pm 0.15	11.98 \pm 0.88	30.87 \pm 2.54	3.71 \pm 0.13
2cylinders	16.46 \pm 0.37	17.93 \pm 1.11	35.81 \pm 0.57	9.35 \pm 0.5
mixed_all	15.7 \pm 0.18	15.95 \pm 0.45	30.69 \pm 0.79	7.22 \pm 1.54
None	57.65 \pm 1.04	50.74 \pm 0.73	57.45 \pm 0.84	22.68 \pm 1.76

Table 4: RMSE if evaluated on **cylinder_stretch**. *None* means that a newly initialized network without any training was evaluated. The lowest RMSE of each column has been marked.

Velocity RMSE $\times 10^{-3}$

Train Dataset	1-step	50-steps	all-steps	all-steps median
standard_cylinder	7.74 ± 0.19	80.62 ± 1.5	163.55 ± 11.32	53.12 ± 10.49
cylinder_stretch	5.48 ± 0.11	84.47 ± 4.18	188.36 ± 3.39	59.97 ± 10.07
cylinder_tri_quad	3.58 ± 0.03	48.09 ± 4.94	154.45 ± 1.73	51.1 ± 5.53
2cylinders	6.81 ± 0.09	77.47 ± 2.13	183.06 ± 3.36	62.54 ± 10.71
mixed_all	3.76 ± 0.06	59.59 ± 7.42	197.34 ± 3.37	63.13 ± 2.65
None	45.22 ± 1.03	624.81 ± 216.15	2032.21 ± 1206.92	2024.38 ± 1217.24

Pressure RMSE $\times 10^{-2}$

Train Dataset	1-step	50-steps	all-steps	all-steps median
standard_cylinder	12.24 ± 0.07	13.8 ± 0.06	20.95 ± 0.33	5.22 ± 0.37
cylinder_stretch	12.48 ± 0.45	14.29 ± 0.17	23.7 ± 0.39	6.59 ± 1.5
cylinder_tri_quad	9.62 ± 0.2	9.96 ± 0.49	18.79 ± 0.7	5.09 ± 0.45
2cylinders	16.35 ± 0.07	19.1 ± 0.29	24.59 ± 0.18	10.21 ± 0.65
mixed_all	14.38 ± 0.26	15.44 ± 1.14	24.04 ± 0.22	8.2 ± 0.47
None	48.06 ± 2.78	46.23 ± 1.45	50.79 ± 0.7	37.96 ± 0.87

Table 5: RMSE if evaluated on **cylinder_tri_quad**. *None* means that a newly initialized network without any training was evaluated. The lowest RMSE of each column has been marked.

Velocity RMSE $\times 10^{-3}$

Train Dataset	1-step	50-steps	all-steps	all-steps median
standard_cylinder	7.79 ± 0.2	54.37 ± 2.64	191.26 ± 10.76	101.61 ± 11.7
cylinder_stretch	7.31 ± 0.06	62.11 ± 2.79	191.01 ± 8.7	110.08 ± 17.34
cylinder_tri_quad	7.01 ± 0.11	61.59 ± 1.03	214.92 ± 13.39	121.21 ± 13.65
2cylinders	3.8 ± 0.03	49.92 ± 2.53	172.97 ± 22.63	86.5 ± 6.04
mixed_all	4.64 ± 0.02	65.34 ± 6.9	198.22 ± 15.02	103.37 ± 10.99
None	47.8 ± 2.06	878.86 ± 177.63	2861.77 ± 457.12	2864.81 ± 472.92

Pressure RMSE $\times 10^{-2}$

Train Dataset	1-step	50-steps	all-steps	all-steps median
standard_cylinder	25.68 ± 0.36	18.73 ± 0.12	31.57 ± 0.78	15.54 ± 0.39
cylinder_stretch	24.8 ± 0.02	18.6 ± 0.09	31.12 ± 0.94	16.77 ± 1.3
cylinder_tri_quad	25.46 ± 0.29	19.85 ± 0.16	33.8 ± 1.34	18.3 ± 1.42
2cylinders	22.43 ± 0.25	20.43 ± 0.31	29.63 ± 1.86	15.51 ± 1.18
mixed_all	23.71 ± 0.33	21.93 ± 0.57	31.96 ± 1.52	18.4 ± 0.76
None	57.04 ± 0.78	53.15 ± 2.59	58.17 ± 1.86	39.02 ± 1.33

Table 6: RMSE if evaluated on **2cylinders**. *None* means that a newly initialized network without any training was evaluated. The lowest RMSE of each column has been marked.

Velocity RMSE $\times 10^{-3}$

Train Dataset	1-step	50-steps	all-steps	all-steps median
standard_cylinder	18.99 ± 0.04	172.27 ± 1.92	305.93 ± 6.97	133.08 ± 7.23
cylinder_stretch	13.0 ± 0.06	175.75 ± 3.76	310.26 ± 1.72	150.07 ± 18.13
cylinder_tri_quad	9.23 ± 0.12	132.15 ± 5.87	320.14 ± 16.5	82.41 ± 17.75
2cylinders	16.27 ± 0.23	184.82 ± 3.45	317.82 ± 11.12	141.39 ± 16.34
mixed_all	7.39 ± 0.1	113.16 ± 3.18	299.35 ± 14.67	92.7 ± 2.04
None	60.08 ± 2.74	956.38 ± 392.02	3394.79 ± 1824.51	3439.83 ± 1862.33

Pressure RMSE $\times 10^{-2}$

Train Dataset	1-step	50-steps	all-steps	all-steps median
standard_cylinder	52.97 ± 0.7	52.41 ± 0.77	68.22 ± 0.94	11.47 ± 0.61
cylinder_stretch	40.59 ± 0.22	47.55 ± 0.62	64.19 ± 0.46	13.83 ± 3.62
cylinder_tri_quad	36.37 ± 0.7	39.12 ± 1.73	61.56 ± 1.79	11.43 ± 3.33
2cylinders	44.38 ± 0.47	54.2 ± 1.05	68.97 ± 0.51	15.95 ± 1.43
mixed_all	32.07 ± 0.39	36.96 ± 0.79	59.23 ± 2.07	14.73 ± 2.27
None	90.13 ± 1.46	80.7 ± 1.71	90.04 ± 1.31	32.46 ± 4.51

Table 7: RMSE if evaluated on **mixed_all**. *None* means that a newly initialized network without any training was evaluated. The lowest RMSE of each column has been marked.

3.3.1 General observations

Before we draw any conclusions, we will put into context what these RMSE values mean. All models produce physically reasonable predictions on every dataset and the following observations apply to all training-evaluation dataset pairs. There are three main ways in which the MGN prediction differs from our FEM simulation.

Firstly, the MGN prediction for all models sometimes does not predict vortex shedding. This is more likely to happen for inflow peaks that are at the border where vortex shedding starts to occur. Fig. 4 shows an example of this. All figures presented in this and the following sections show only the pressure or velocity field prediction at the final time step. However, for each figure, we uploaded the full simulation animation as a gif file to this work’s GitHub repository [65].

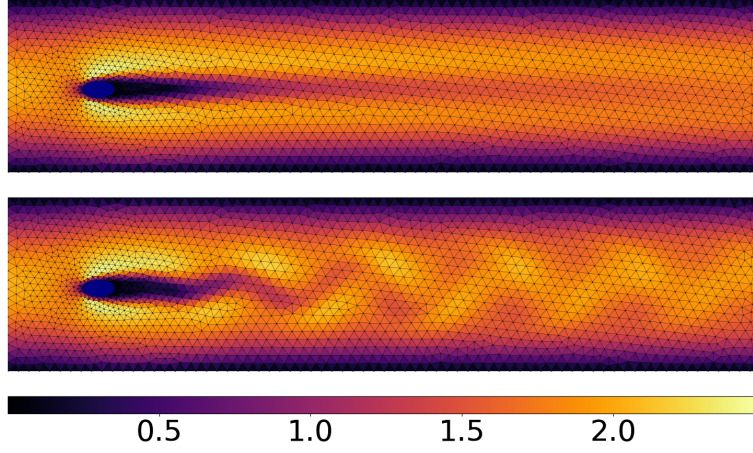


Figure 4: Plot of the Euclidean norm of the velocity field at the final time step for a FEM simulation (bottom) and the corresponding MGN prediction (top) of a mesh coming from the **cylinder_stretch** dataset. The prediction has an all-steps RMSE of circa 0.076 and stems from an MGN that was trained on **cylinder_stretch**.

Secondly, the MGN sometimes fails to estimate the propagation speed of the vortices. This causes the MGN prediction to look out of sync at later time steps. This is especially prevalent for high inflow peaks. Fig. 5 shows two examples of this. Fig. 5 also demonstrates that the RMSE does not always capture how qualitatively wrong the prediction is as a higher inflow peak causes the average magnitude of the velocity field and thereby its error to be higher.

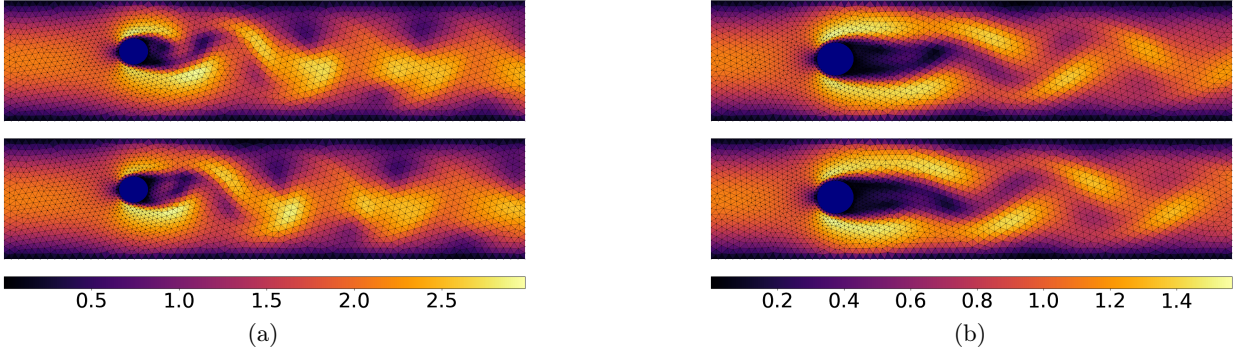


Figure 5: Plot of the Euclidean norm of the velocity field at the final time step for two FEM simulations (bottom) and their corresponding MGN predictions (top) of two meshes coming from the **standard_cylinder** dataset. The prediction (a) has an all-steps RMSE of circa 0.193 and (b) has an all-steps RMSE of circa 0.086. Both predictions stem from an MGN that was trained on **standard_cylinder**.

Thirdly, when the MGN (and this is mostly the case for unseen shapes) predicts vortex shedding, it predicts a wrong pattern of the vortices. Fig. 6 shows an example of this.

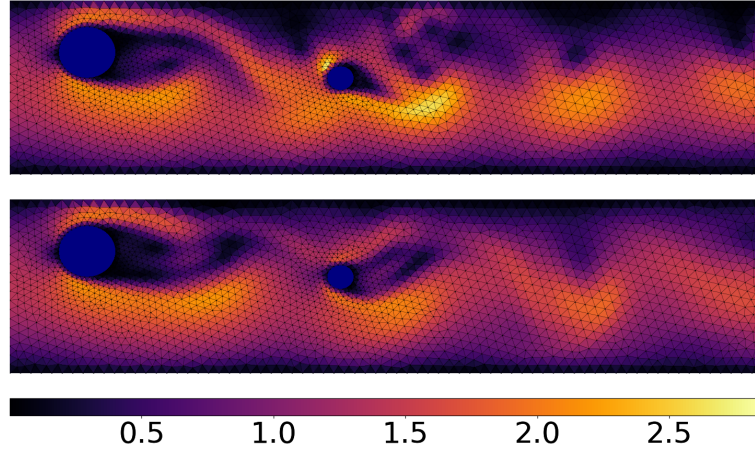


Figure 6: Plot of the Euclidean norm of the velocity field at the final time step for a FEM simulation (bottom) and the corresponding MGN prediction (top) of a mesh coming from the **2cylinders** dataset. The prediction has an all-steps RMSE of circa 0.318 and stems from an MGN that was trained on **standard_cylinder**. Note that the vortex pattern at the smaller circle differs from the IPCS solution as the MGN predicts pairs of vortices whereas the IPCS does not.

Unsurprisingly, all models thrive in handling the low inflow peak regime where no vortex shedding occurs. Fig. 7 shows an example of this.

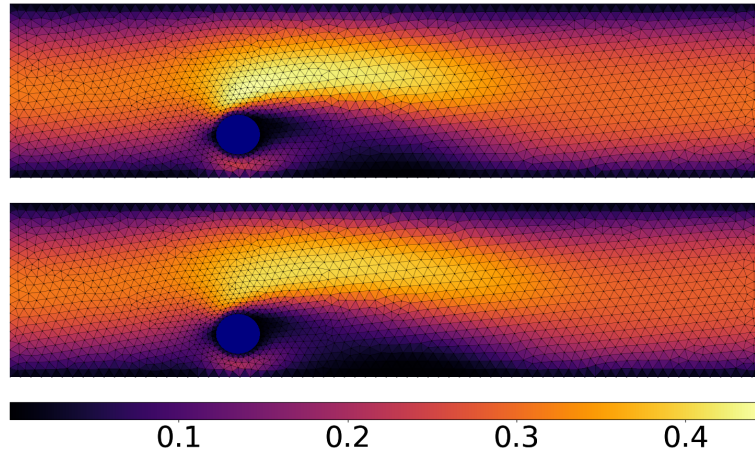


Figure 7: Plot of the Euclidean norm of the velocity field at the final time step for a FEM simulation (bottom) and the corresponding MGN prediction (top) of a mesh coming from the **standard_cylinder** dataset. The prediction has an all-steps RMSE of circa 0.012 and stems from an MGN that was trained on **standard_cylinder**.

Thus far we have only shown the velocity field and not the pressure field. This is because the pressure field is uninteresting as its deviation from the FEM pressure solution directly correlates with the deviation from the velocity field since the MGN directly predicts the pressure from the velocity field. Fig. 8 shows the pressure field together with the velocity field and their prediction for an average **cylinder_flow** instance.

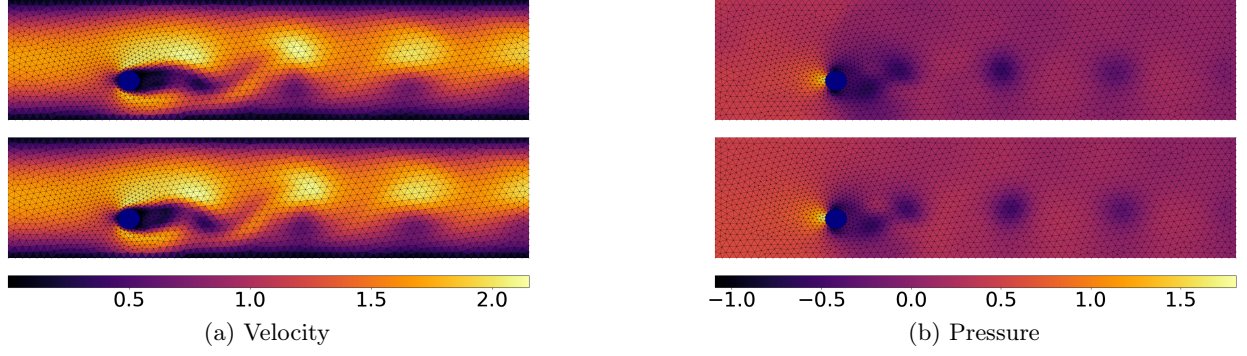


Figure 8: Plot of the pressure field (right) and the Euclidean norm of the velocity field (left) at the final time step for a FEM simulation (bottom) and its corresponding MGN prediction (top) of one mesh coming from the **standard_cylinder** dataset. The velocity prediction (a) has an all-steps RMSE of roughly 0.032 and the pressure prediction (b) has an all-steps RMSE of approximately 0.016. Both predictions stem from an MGN that was trained on **standard_cylinder**.

3.3.2 Predictions for coinciding train and test datasets

We observed that if the MGN is trained on the same dataset it is evaluated on and it predicts vortex shedding, then these vortices have mostly the same characteristics as the IPCS solution which is only partially the case for differing train and evaluation datasets as we shall see later. Fig. 9 shows one simulation and its prediction for each of the five datasets when the network was trained on the same dataset. The simulations were picked to have an RMSE near the RMSE median for that dataset.

3.3.3 Predictions for differing train and test datasets

Though the RMSE values in all metrics do not differ much in relative terms between different training-evaluation dataset pairs, we can observe discrepancies when looking at the simulations. Fig. 10 shows predictions of a model trained on **standard_cylinder** and evaluated on a selection of simulations from different datasets. This figure shows that if vortex shedding is predicted, it is essentially a coin flip whether the correct vortex pattern is predicted on a previously unseen shape. This is not reflected in the RMSE as an out-of-sync but characteristically correct vortex prediction can have the same RMSE as a straight-up wrong pattern.

3.3.4 Intermediate conclusions

Judging purely from the reported RMSE values, one could argue that MGNs generalize well for all training-evaluation dataset pairs. All training-evaluation dataset pairs' velocity RMSE is almost always an order of magnitude below what a freshly initialized MGN would produce in all metrics. For most datasets (unsurprisingly) the model that was evaluated and trained on the same dataset performs best. However, the other models which were trained on different datasets perform only slightly worse in relative terms.

In general, MGNs are strong at predicting flow on a coarse level, therefore they almost always produce a physically reasonable prediction even for unseen shapes. However, their main weakness is

correctly predicting the vortex patterns which is arguably the most difficult and interesting part of the prediction. This problem is more likely to occur when the mesh contains a shape that was never seen in training. However, we do note that though not always, MGNs can oftentimes correctly predict a vortex pattern for a shape that was not seen in training.

Given that our experiment setup is not optimal since one could use a larger MGN, finer meshes, more precisely generated datasets, one could achieve a significantly higher accuracy which is likely to translate to the generalization tasks. Therefore, one has to take into consideration that these experiments do not show the full potential of MGNs.

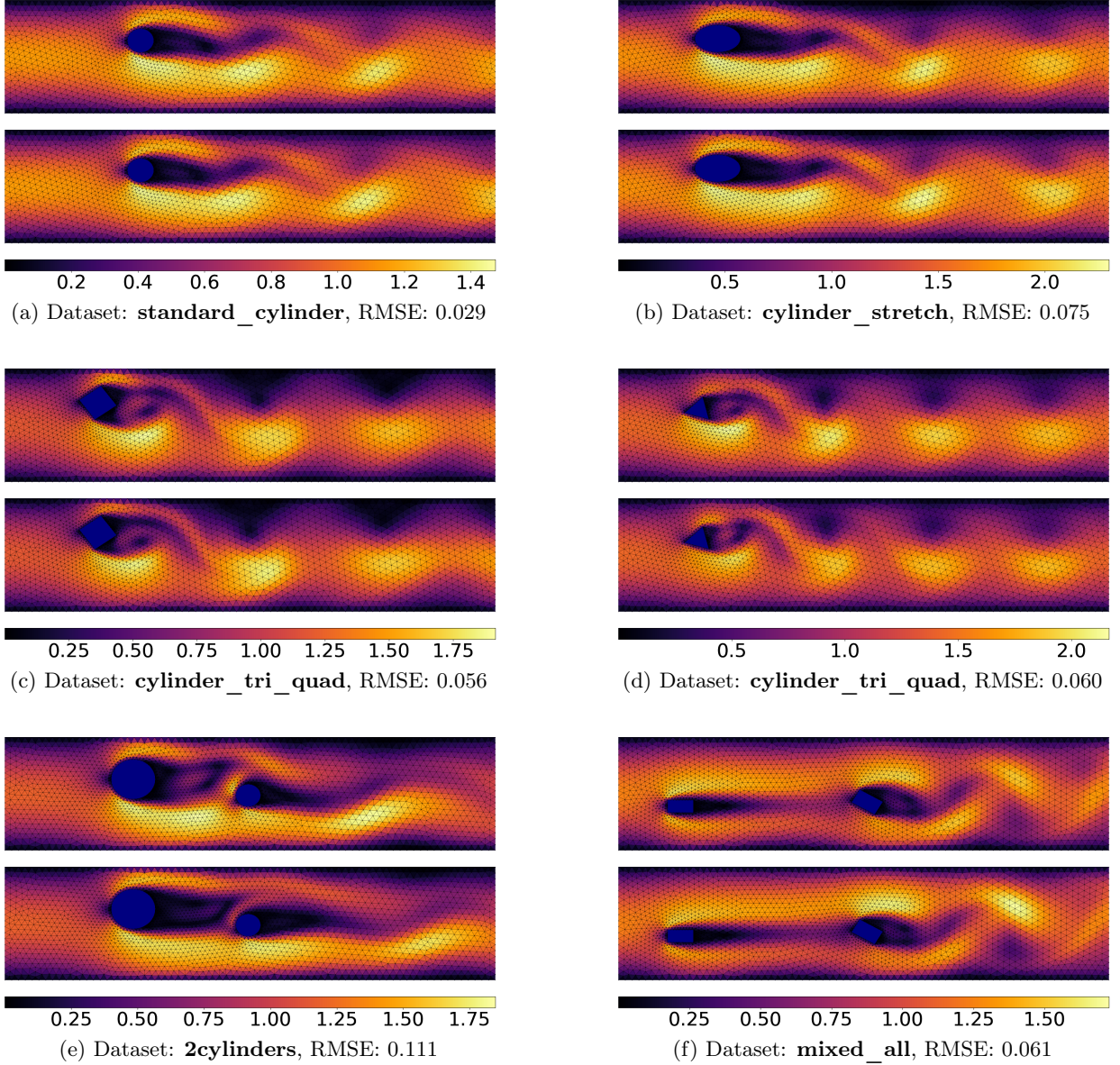
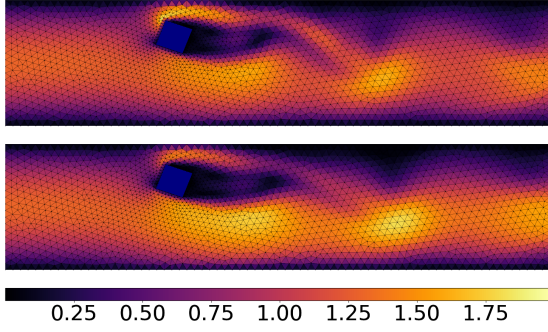
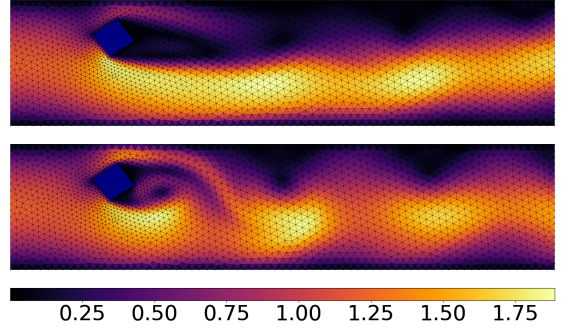


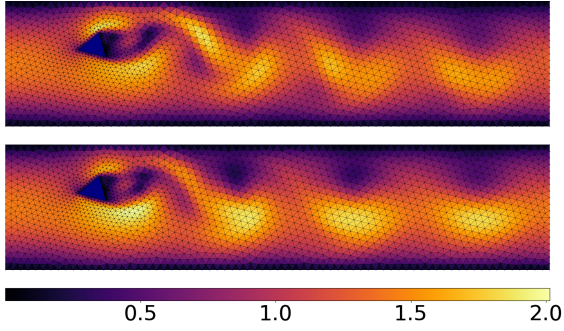
Figure 9: Plot of the Euclidean norm of the velocity field at the final time step for six FEM simulations (bottom) and their corresponding MGN predictions (top) of six meshes coming from the dataset mentioned in the corresponding subcaption. Each subcaption also contains the all-steps RMSE for the corresponding simulation rounded to three decimal places. The predictions stem from MGNs that were trained on the same dataset on which the predictions were performed.



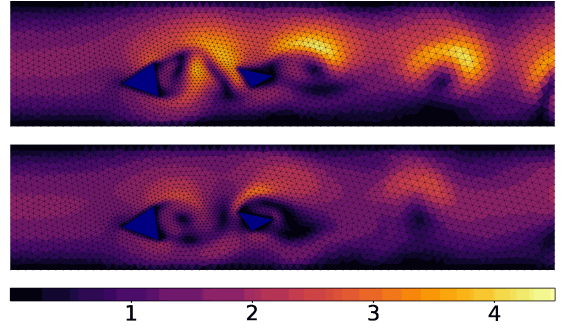
(a) Dataset: **cylinder_tri_quad**, RMSE: 0.118. Vortex pattern **correctly** predicted.



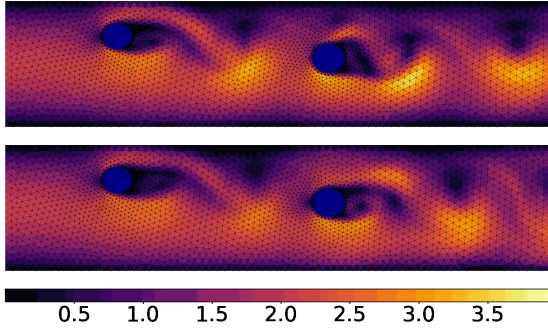
(b) Dataset: **cylinder_tri_quad**, RMSE: 0.196. Vortex pattern **falsely** predicted.



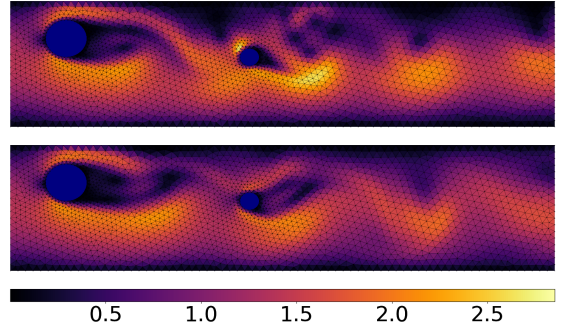
(c) Dataset: **cylinder_tri_quad**, RMSE: 0.197. Vortex pattern **correctly** predicted.



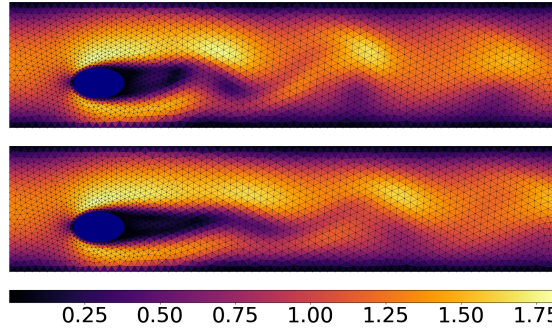
(d) Dataset: **mixed_all**, RMSE: 0.558. Vortex pattern **falsely** predicted.



(e) Dataset: **2cylinders**, RMSE: 0.389. Vortex pattern **correctly** predicted.



(f) Dataset: **2cylinders**, RMSE: 0.318. Vortex pattern **falsely** predicted.



(g) Dataset: **cylinder_stretch**, RMSE: 0.055. Vortex pattern **correctly** predicted.

Figure 10: Plot of the Euclidean norm of the velocity field at the final time step for three FEM simulations (bottom) and their corresponding MGN predictions (top) of six meshes coming from the dataset mentioned in the corresponding subcaption. Each subcaption also contains the all-steps RMSE for the corresponding simulation rounded to three decimal places. All predictions stem from the same MGN that was trained on **standard_cylinder**.

3.4 Generalization experiments: Runtimes

In this section, we compare the runtime of an MGN to that of the IPCS on **standard_cylinder** using the implementation and hyperparameters we described in the experiment setup. For the MGN we differentiate between using a GPU and only using a CPU. The aim is to find the number of simulations one wants to generate at which it is computationally more efficient to use an MGN over the IPCS. All runtimes reported in the following are extrapolations.

Firstly, we consider the case where we only use a CPU. In this case, we consider a system with six Intel(R) Core(TM) i5-9600K @ 3.70GHz CPUs with 32 GB of RAM. Using this system, we need roughly 0.3125h to generate a single simulation using the IPCS which results in circa 125h to generate the entire **standard_cylinder** train dataset. We then need roughly 1138h to train the MGN and then approximately 0.048h to generate a new simulation using the MGN. At inference time, this is an approximately **6.5 times speedup**.

Next, we consider the case where we have access to a GPU for training and inference of the MGN. Keeping everything as above and using the Alienware m17 R5 AMD laptop with the GeForce RTX 3070 Ti as the GPU with 8 GB of RAM only for the MGN training and inference, we get a total MGN training time of roughly 58h and then approximately 0.0031h to generate a new simulation. At inference time, this is an approximately **100.8 times speedup**.

4 Conclusion

In this work, we investigated MGNs by extending the generalization experiments of DeepMind [54] by evaluating MGNs on meshes with previously unseen shapes. For this, we first created five datasets **standard_cylinder**, **cylinder_stretch**, **cylinder_tri_quad**, **2cylinders**, and **mixed_all**, which contain simulations of fluid flow around one or two objects of different shapes. We showed that MGNs in general can produce physically reasonable predictions for meshes with unseen shapes. Additionally, our MGNs managed to correctly predict vortex patterns for many unseen shapes. However, when a shape has not yet been seen in training the MGN is equally likely to falsely predict the vortex pattern for inflow peaks at which vortex shedding occurs. Nevertheless, for many engineering applications it is sufficient to have a coarse approximation of the flow field and the inference of the MGN is in our simulations up to 100 times faster than the classical numerical solver.

In the future, one could consider differently shaped domains as opposed to the rectangular one chosen here and other fluid benchmark problems like lid-driven cavity or backward facing step. Additionally, one could also consider adding system parameters like the viscosity to the MGN and consider varying it during training and see how well the MGN generalizes in this case.

5 Declarations

5.1 Availability of data and material

The code for this article is available at <https://github.com/codebro634/modulus> [65]. All other data will be made available on reasonable request.

5.2 Competing interests

The authors declare that they have no known competing financial interests or personal relationships that could have appeared to influence the work reported in this paper.

5.3 Funding and acknowledgements

The third and fourth authors acknowledge the funding of the German Research Foundation (DFG) within the framework of the International Research Training Group on Computational Mechanics Techniques in High Dimensions GRK 2657 under Grant Number 433082294. The second author acknowledges support by an ETH Zurich Postdoctoral Fellowship.

5.4 Credit Authorship Contribution Statement

R. Schmöcker: Conceptualization, Methodology, Software, Validation, Formal analysis, Investigation, Writing – original draft, Visualization.
A. Henkes: Validation, Formal analysis, Investigation, Writing – original draft, Writing – review & editing, Advisory.
J. Roth: Conceptualization, Methodology, Validation, Formal analysis, Investigation, Writing – original draft, Writing – review & editing, Visualization, Supervision.
T. Wick: Conceptualization, Formal analysis, Resources, Writing - review & editing, Supervision, Funding acquisition.

References

- [1] C. C. Aggarwal. *Neural Networks and Deep Learning: A Textbook*. Springer International Publishing, 2018.
- [2] K. R. Allen, T. Lopez-Guevara, K. L. Stachenfeld, A. Sanchez-Gonzalez, P. W. Battaglia, J. B. Hamrick, and T. Pfaff. Inverse Design for Fluid-Structure Interactions using Graph Network Simulators. In *Neural Information Processing Systems*, 2022.
- [3] M. S. Alnaes, J. Blechta, J. Hake, A. Johansson, B. Kehlet, A. Logg, C. Richardson, J. Ring, M. E. Rognes, and G. N. Wells. The FEniCS Project Version 1.5. *Archive of Numerical Software*, 3, 2015.

- [4] D. Amsallem, M. J. Zahr, and C. Farhat. Nonlinear model order reduction based on local reduced-order bases. *Int. J. Numer. Methods Eng.*, 92(10):891–916, 2012.
- [5] M. Anselmann and M. Bause. A Geometric Multigrid Method for Space-Time Finite Element Discretizations of the Navier–Stokes Equations and its Application to 3D Flow Simulation. *ACM Trans. Math. Softw.*, 49(1), mar 2023.
- [6] D. Arndt, N. Fehn, G. Kanschat, K. Kormann, M. Kronbichler, P. Munch, W. A. Wall, and J. Witte. ExaDG: High-Order Discontinuous Galerkin for the Exa-Scale. In H.-J. Bungartz, S. Reiz, B. Uekermann, P. Neumann, and W. E. Nagel, editors, *Software for Exascale Computing - SPPEXA 2016-2019*, pages 189–224, Cham, 2020. Springer International Publishing.
- [7] P. Astrid, S. Weiland, K. Willcox, and T. Backx. Missing Point Estimation in Models Described by Proper Orthogonal Decomposition. *IEEE Trans. Autom. Control*, 53:2237–2251, 2008.
- [8] J. L. Ba, J. R. Kiros, and G. E. Hinton. Layer Normalization, 2016. <https://doi.org/10.48550/arXiv.1607.06450>.
- [9] M. Barrault, Y. Maday, N. Nguyen, and A. Patera. An ‘empirical interpolation’ method: application to efficient reduced-basis discretization of partial differential equations. *C.R. Math.*, 339:667–672, 2004.
- [10] R. Becker and R. Rannacher. An optimal control approach to a posteriori error estimation in finite element methods. *Acta Numerica*, 10:1–102, 2001.
- [11] M. Besier and R. Rannacher. Goal-oriented space-time adaptivity in the finite element Galerkin method for the computation of nonstationary incompressible flow. *Int. J. Num. Meth. Fluids*, 70:1139–1166, 2012.
- [12] C. M. Bishop. *Pattern recognition and machine learning*. Springer, 2006.
- [13] F. Bonnet, J. A. Mazari, T. Munzer, P. Yser, and P. Gallinari. An extensible Benchmarking Graph-Mesh dataset for studying Steady-State Incompressible Navier-Stokes Equations. In *ICLR 2022 Workshop on Geometrical and Topological Representation Learning*, 2022.
- [14] M. Braack and T. Richter. Solutions of 3D Navier–Stokes benchmark problems with adaptive finite elements. *Comput. Fluids*, 35(4):372–392, 2006.
- [15] T. Bricken, A. Templeton, J. Batson, B. Chen, A. Jermyn, T. Conerly, N. Turner, C. Anil, C. Denison, A. Askell, R. Lasenby, Y. Wu, S. Kravec, N. Schiefer, T. Maxwell, N. Joseph, Z. Hatfield-Dodds, A. Tamkin, K. Nguyen, B. McLean, J. E. Burke, T. Hume, S. Carter, T. Henighan, and C. Olah. Towards Monosemanticity: Decomposing Language Models With Dictionary Learning. *Transformer Circuits Thread*, 2023. <https://transformer-circuits.pub/2023/monosemantic-features/index.html>.

- [16] M. M. Bronstein, J. Bruna, T. Cohen, and P. Veličković. Geometric Deep Learning: Grids, Groups, Graphs, Geodesics, and Gauges, 2021. <https://doi.org/10.48550/arXiv.2104.13478>.
- [17] M. M. Bronstein, J. Bruna, Y. LeCun, A. Szlam, and P. Vandergheynst. Geometric Deep Learning: Going beyond Euclidean data. *IEEE Signal Processing Magazine*, 34(4):18–42, 2017.
- [18] S. Cai, Z. Mao, Z. Wang, M. Yin, and G. E. Karniadakis. Physics-informed neural networks (PINNs) for fluid mechanics: a review. *Acta Mech. Sin.*, 37(12):1727–1738, Dec 2021.
- [19] S. Chaturantabut and D. Sorensen. Nonlinear Model Reduction via Discrete Empirical Interpolation. *SIAM J. Sci. Comput.*, 32:2737–2764, 2010.
- [20] S. Chaturantabut and D. Sorensen. A State Space Error Estimate for POD-DEIM Nonlinear Model Reduction. *SIAM J. Numer. Anal.*, 50:46–63, 2012.
- [21] J. Chen, E. Hachem, and J. Viquerat. Graph neural networks for laminar flow prediction around random two-dimensional shapes. *Phys. Fluids*, 33(12):123607, 12 2021.
- [22] F. Chollet. *Deep Learning with Python*, volume 361. Manning New York, 2018.
- [23] A. J. Chorin. Numerical Solution of the Navier-Stokes Equations. *Math. Comput.*, 22(104):745–762, 1968.
- [24] Z. Drmač and S. Gugercin. A New Selection Operator for the Discrete Empirical Interpolation Method—Improved A Priori Error Bound and Extensions. *SIAM J. Sci. Comput.*, 38(2):A631–A648, 2016.
- [25] H. Elman, D. Silvester, and A. Wathen. *Finite Elements and Fast Iterative Solvers*. Oxford University Press, 2014.
- [26] D. Erhan, Y. Bengio, A. Courville, and P. Vincent. Visualizing Higher-Layer Features of a Deep Network. *Technical Report, Univeristé de Montréal*, 01 2009.
- [27] M. Fortunato, T. Pfaff, P. Wirsberger, A. Pritzel, and P. Battaglia. MultiScale MeshGraphNets. In *ICML 2022 2nd AI for Science Workshop*, 2022.
- [28] G. Galdi. *An Introduction to the Mathematical Theory of the Navier-Stokes Equations: Steady-State Problems*. Springer Monographs in Mathematics. Springer New York, 2011.
- [29] A. Géron. *Hands-on machine learning with Scikit-Learn, Keras, and TensorFlow: Concepts, tools, and techniques to build intelligent systems*. O’Reilly Media, 2019.
- [30] V. Girault and P.-A. Raviart. *Finite Element method for the Navier-Stokes equations*. Number 5 in Computer Series in Computational Mathematics. Springer-Verlag, 1986.
- [31] R. Glowinski. Finite element methods for incompressible viscous flow. In *Numerical Methods for Fluids (Part 3)*, volume 9 of *Handbook of Numerical Analysis*, pages 3–1176. Elsevier, 2003.

- [32] I. Goodfellow, Y. Bengio, A. Courville, and Y. Bengio. *Deep learning*, volume 1. MIT press Cambridge, 2016.
- [33] C. Gräkle, M. Hinze, J. Lang, and S. Ullmann. POD model order reduction with space-adapted snapshots for incompressible flows. *Adv. Comput. Math.*, 45:2401–2428, 2019.
- [34] V. Grimm, A. Heinlein, and A. Klawonn. Learning the solution operator of two-dimensional incompressible Navier-Stokes equations using physics-aware convolutional neural networks, 2023. <https://doi.org/10.48550/arXiv.2308.02137>.
- [35] M. B. Hauser. Principles of Riemannian geometry in neural networks. *PhD thesis*, 2018.
- [36] O. Hennigh, S. Narasimhan, M. A. Nabian, A. Subramaniam, K. Tangsali, M. Rietmann, J. del Aguila Ferrandis, W. Byeon, Z. Fang, and S. Choudhry. NVIDIA SimNet: an AI-accelerated multi-physics simulation framework, 2020. <https://doi.org/10.48550/arXiv.2012.07938>.
- [37] J. Hesthaven and S. Ubbiali. Non-intrusive reduced order modeling of nonlinear problems using neural networks. *J. Comput. Phys.*, 363:55–78, 2018.
- [38] K. Hornik, M. Stinchcombe, and H. White. Multilayer feedforward networks are universal approximators. *Neural networks*, 2(5):359–366, 1989.
- [39] V. John. A comparison of parallel solvers for the incompressible Navier–Stokes equations. *Comput. Visualization Sci.*, 1(4):193–200, Jul 1999.
- [40] V. John. *Finite Element Methods for Incompressible Flow Problems*. Springer, 2016.
- [41] A. U. Kennington. Differential geometry reconstructed: a unified systematic framework. <http://www.topology.org/tex/conc/dg.html>, 2024.
- [42] D. Kochkov, J. A. Smith, A. Alieva, Q. Wang, M. P. Brenner, and S. Hoyer. Machine learning-accelerated computational fluid dynamics. *PNAS*, 118(21):e2101784118, 2021.
- [43] A. Krizhevsky, I. Sutskever, and G. E. Hinton. Imagenet classification with deep convolutional neural networks. In F. Pereira, C. Burges, L. Bottou, and K. Weinberger, editors, *Advances in Neural Information Processing Systems*, volume 25. Curran Associates, Inc., 2012.
- [44] J. N. Kutz. Deep learning in fluid dynamics. *J. Fluid Mech.*, 814:1–4, 2017.
- [45] R. Lam, A. Sanchez-Gonzalez, M. Willson, P. Wirnsberger, M. Fortunato, F. Alet, S. Ravuri, T. Ewalds, Z. Eaton-Rosen, W. Hu, A. Merose, S. Hoyer, G. Holland, O. Vinyals, J. Stott, A. Pritzel, S. Mohamed, and P. Battaglia. Learning skillful medium-range global weather forecasting. *Science*, 382(6677):1416–1421, 2023.
- [46] H. P. Langtangen and A. Logg. *Solving PDEs in Python*. Simula SpringerBriefs on Computing. Springer Cham, 1 edition, 2017.

- [47] Z. Li, N. B. Kovachki, C. Choy, B. Li, J. Kossaifi, S. P. Otta, M. A. Nabian, M. Stadler, C. Hundt, K. Azizzadenesheli, and A. Anandkumar. Geometry-Informed Neural Operator for Large-Scale 3D PDEs. In *Thirty-seventh Conference on Neural Information Processing Systems*, 2023.
- [48] N. Margenberg, D. Hartmann, C. Lessig, and T. Richter. A neural network multigrid solver for the Navier-Stokes equations. *J. Comput. Phys.*, 460:110983, 2022.
- [49] S. Mittal, A. Ratner, D. Hastreiter, and T. Tezduyar. Space-time finite element computation of incompressible flows with emphasis on flow involving oscillating cylinders. *Internat. Video J. Engrg. Res.*, 1:83–86, 1991.
- [50] F. Moukalled, L. Mangani, and M. Darwish. *The Finite Volume Method in Computational Fluid Dynamics*. Springer, 2016.
- [51] N. Nguyen, A. Patera, and J. Peraire. A ‘best points’ interpolation method for efficient approximation of parametrized function. *Int. J. Numer. Methods Eng.*, 73:521 – 543, 01 2008.
- [52] R. Novak, Y. Bahri, D. A. Abolafia, J. Pennington, and J. Sohl-Dickstein. Sensitivity and Generalization in Neural Networks: an Empirical Study. In *International Conference on Learning Representations*, 2018.
- [53] NVIDIA Modulus Team. NVIDIA Modulus. <https://github.com/NVIDIA/modulus/tree/main>.
- [54] T. Pfaff, M. Fortunato, A. Sanchez-Gonzalez, and P. Battaglia. Learning Mesh-Based Simulation with Graph Networks. In *International Conference on Learning Representations*, 2021.
- [55] R. Rannacher. *Finite Element Methods for the Incompressible Navier-Stokes Equations*, pages 191–293. Birkhäuser Basel, Basel, 2000.
- [56] J. Roth, J. P. Thiele, U. Köcher, and T. Wick. Tensor-Product Space-Time Goal-Oriented Error Control and Adaptivity With Partition-of-Unity Dual-Weighted Residuals for Nonstationary Flow Problems. *Comput. Methods Appl. Math.*, 24(1):185–214, 2024.
- [57] G. Rozza, D. B. P. Huynh, and A. T. Patera. Reduced basis approximation and a posteriori error estimation for affinely parametrized elliptic coercive partial differential equations. *Arch. Comput. Methods Eng.*, 15(3):1–47, Sep 2007.
- [58] G. Rozza, G. Stabile, and F. Ballarin. *Advanced Reduced Order Methods and Applications in Computational Fluid Dynamics*. Society for Industrial and Applied Mathematics, Philadelphia, PA, 2022.
- [59] A. Sanchez-Gonzalez, J. Godwin, T. Pfaff, R. Ying, J. Leskovec, and P. Battaglia. Learning to Simulate Complex Physics with Graph Networks. In H. D. III and A. Singh, editors, *Proceedings of the 37th International Conference on Machine Learning*, volume 119 of *Proceedings of Machine Learning Research*, pages 8459–8468. PMLR, 13–18 Jul 2020.

- [60] B. Sanchez-Lengeling, E. Reif, A. Pearce, and A. B. Wiltschko. A Gentle Introduction to Graph Neural Networks. *Distill*, 2021. <https://distill.pub/2021/gnn-intro>.
- [61] N. Schlömer. pygmsh: A Python frontend for Gmsh. <https://github.com/nschloe/pygmsh> [Last accessed 10.05.2024], 2018.
- [62] M. Schäfer, S. Turek, F. Durst, E. Krause, and R. Rannacher. Benchmark Computations of Laminar Flow Around a Cylinder. *Vieweg+Teubner Verlag*, pages 547–566, 1996.
- [63] K. Simonyan, A. Vedaldi, and A. Zisserman. Deep Inside Convolutional Networks: Visualising Image Classification Models and Saliency Maps. In *Workshop at International Conference on Learning Representations*, 2014.
- [64] H. Tang and Y. Liu. Towards Understanding Generalization of Graph Neural Networks. In *International Conference on Machine Learning*, 2023.
- [65] K. Tangsali, M. A. Nabian, N. Geneva, R. Schmöcker, A. Subramaniam, D. Foster, O. Hennigh, D. Pruitt, M. Stadler, R. Cherukuri, M. Koch, S. Wang, N. D. Brenowitz, A. Kamenev, B. M. L. Borgne, J. Yang, L. Pegolotti, M. Mardani, S. Jones, S. Roy, and T. Kurth. codebro634/modulus: v1.0.0. <https://doi.org/10.5281/zenodo.11504394>, June 2024.
- [66] R. Temam. *Navier-Stokes Equations: Theory and Numerical Analysis*. AMS/Chelsea publication. AMS Chelsea Pub., 2001.
- [67] T. E. Tezduyar, M. Behr, S. Mittal, and A. A. Johnson. *Computation of unsteady incompressible flows with the Finite Element Methods Space-Time Formulations, Iterative Strategies and Massively Parallel Implementations*, volume 143 of *New Methods in Transient Analysis, PVP-Vol. 246, AMD-Vol. 143*, pages 7–24. ASME, New York, 1992.
- [68] S. Turek. *Efficient Solvers for Incompressible Flow Problems: An Algorithmic and Computational Approach*. Lecture Notes in Computational Science and Engineering. Springer-Verlag, 1999.
- [69] H. Wu, H. Luo, H. Wang, J. Wang, and M. Long. Transolver: A Fast Transformer Solver for PDEs on General Geometries. In *International Conference on Machine Learning*, 2024.
- [70] M. D. Zeiler and R. Fergus. Visualizing and Understanding Convolutional Networks. In D. Fleet, T. Pajdla, B. Schiele, and T. Tuytelaars, editors, *Computer Vision – ECCV 2014*, pages 818–833, Cham, 2014. Springer International Publishing.